ACS Catalysis

pubs.acs.org/acscatalysis

Research Article

Effect of the Morphology of the High-Surface-Area Support on the Performance of the Oxygen-Evolution Reaction for Iridium Nanoparticles

Leonard Moriau, Marjan Bele, Živa Marinko, Francisco Ruiz-Zepeda, Gorazd Koderman Podboršek, Martin Šala, Angelja Kjara Šurca, Janez Kovač, Iztok Arčon, Primož Jovanovič,* Nejc Hodnik,* and Luka Suhadolnik*

Cite This: *ACS Catal.* 2021, 11, 670−681

Read Online

ACCESS | Metrics & More | Article Recommendations | Supporting Information

ABSTRACT: The development of affordable, low-iridium-loading, scalable, active, and stable catalysts for the oxygen-evolution reaction (OER) is a requirement for the commercialization of proton-exchange membrane water electrolyzers (PEMWEs). However, the synthesis of high-performance OER catalysts with minimal use of the rare and expensive element Ir is very challenging and requires the identification of electrically conductive and stable high-surface-area support materials. We developed a synthesis procedure for the production of large quantities of a nanocomposite powder containing titanium oxynitride ($TiON_x$) and Ir. The catalysts were synthesized with an anodic oxidation process followed by detachment, milling, thermal treatment, and the deposition of Ir nanoparticles. The anodization time was varied to grow three different types of nanotubular structures exhibiting different lengths and wall thicknesses and thus a variety of properties. A comparison of milled samples with different degrees of nanotubular clustering and morphology retention, but with identical chemical compositions and Ir nanoparticle size distributions and dispersions, revealed that the nanotubular support morphology is the determining factor governing the catalyst's OER activity and stability. Our study is supported by various state-of-the-art materials' characterization techniques, like X-ray photoelectron spectroscopy, scanning and transmission electron microscopies, X-ray powder diffraction and absorption spectroscopy, and electrochemical cyclic voltammetry. Anodic oxidation proved to be a very suitable way to produce high-surface-area powder-type catalysts as the produced material greatly outperformed the IrO_2 benchmarks as well as the Ir-supported samples on morphologically different $TiON_x$ from previous studies. The highest activity was achieved for the sample prepared with 3 h of anodization, which had the most appropriate morphology for the effective removal of oxygen bubbles.

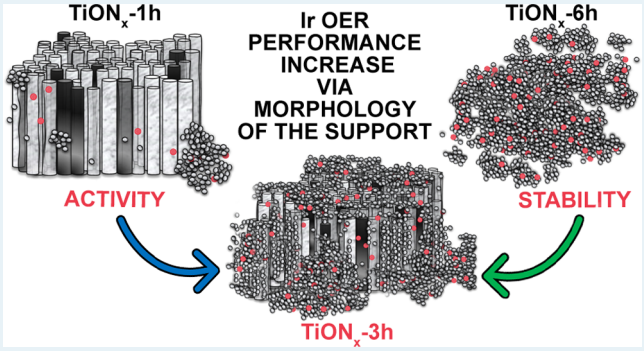

KEYWORDS: *electrocatalysis, oxygen-evolution reaction, $TiON_x$-Ir powder catalyst, iridium nanoparticles, anodic oxidation, morphology−activity correlation*

1. INTRODUCTION

The hydrogen cycle is a promising way to store energy from renewable sources, like solar and wind, through the splitting of water in an electrolyzer. This energy can subsequently be made available on-demand using a fuel cell that combines the hydrogen and the oxygen.[1] However, the efficiency of the water-splitting reaction is limited by the slow kinetics of the oxygen-evolution reaction (OER).[2] Indeed, even with a state-of-the-art catalyst in acidic media, i.e., IrO_2, an overpotential of around 0.3 V is usually required to achieve proper current densities.[3] Moreover, iridium is a precious and scarce metal, which hinders the commercialization of this technology. One way to decrease the cost of the device is to improve the utilization of the iridium. An example of this is the deposition of iridium in the form of nanoparticles on a suitable support.[4] This makes it possible to lower the cost as well as to potentially improve the catalyst's performance, which, together with the properties of the catalytically active sites, strongly depends on the interactions with the support. The so-called strong metal−support interaction (SMSI), mostly known from heterogeneous catalysis, was shown to also affect the structural and

Received: October 31, 2020
Revised: December 16, 2020
Published: December 30, 2020

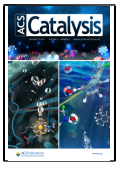

chemical changes of the electrocatalyst during the OER.[5,6] The most commonly used support in electrocatalysis is carbon;[7−9] however, several new materials have been proposed[10−12] to address its shortcoming, i.e., poor stability under OER electrochemical conditions.[13] One of the challenges with OER electrocatalysts is to find an appropriate substitute for the traditional carbon support. It must be replaced by a large-surface-area support with a high-enough electrical conductivity, so it does not negatively affect the catalyst's performance. Additionally, the stability and electronic catalyst−support interactions, as well as the economic criteria, need to be taken into account.[11,14−16] Given the stated requirements, a promising substitute for carbon is titanium oxynitride ($TiON_x$), which can be prepared from titanium dioxide (TiO_2)[17] or titanium nitride (TiN)[18] in the form of various nanostructures.[19−21] There are different synthesis methods to choose from. Radio frequency (RF) plasma can be used for the oxynitridation of titanium;[22] the mechanical milling of titanium powder in air results in the formation of titanium oxynitride;[23] and low-pressure chemical vapor deposition (LPCVD) can be used to deposit titanium oxynitride on silicon substrates.[24] Of the possible synthesis processes, one of the most direct and controllable is to synthesize TiO_2 nanostructures, which are then thermally treated in a reductive ammonia atmosphere (above 600 °C) to transform the TiO_2 to $TiON_x$.[25] The anodic oxidation of titanium is commonly used for the synthesis of immobilized nanotubular films.[26] It results in TiO_2 nanotube arrays that are firmly adhered to the titanium substrate[27] and has been used to fabricate free-standing TiO_2 membranes[28] and TiO_2 nanotube powders.[29] Before the prepared TiO_2 nanotube powders can be used as a support for Ir nanoparticles, their electrical conductivity has to be substantially increased. This can be achieved with a thermal treatment in an ammonia atmosphere. The final step of the OER catalyst's preparation, i.e., the deposition of Ir in the form of finely dispersed, ultrasmall nanoparticles, was already demonstrated by our group.[30−32] In this investigation, we developed a new, anodic, oxidation-based synthesis process for the cost-effective fabrication of high-performance OER $TiON_x$-Ir nanopowder electrocatalysts. The influence of the anodization time on the catalyst's support morphology, structure, and composition was studied in detail using various state-of-the-art characterization methods, such as X-ray photoelectron spectroscopy (XPS), scanning electron microscopy (SEM), scanning transmission electron microscopy (STEM), X-ray diffraction (XRD), and extended X-ray absorption fine structure (EXAFS). We show that the electrochemical activity and stability can be substantially enhanced, compared to the commercial benchmark IrO_2 material and to the other best OER catalysts in the literature, exclusively by modifying the $TiON_x$ support morphology.

2. EXPERIMENTAL SECTION

2.1. Synthesis of $TiON_x$-Ir Catalysts. The $TiON_x$-Ir catalyst was prepared by following the procedure schematically shown in Figure 1. In the first step, titanium foil (200 μm thick, 99.8%, Baoji Lyne Metals Co., Ltd.) was cleaned with acetone and ethanol in an ultrasonic bath and then anodized in an electrolyte consisting of 0.3 wt % NH_4F (99.99%, Sigma-Aldrich) and 2 vol % deionized water in ethylene glycol (99.5%, Carlo Erba Reagents). The foil was anodized at a constant potential of 60 V in a two-electrode electrochemical cell using a stainless steel counter electrode. The anodization

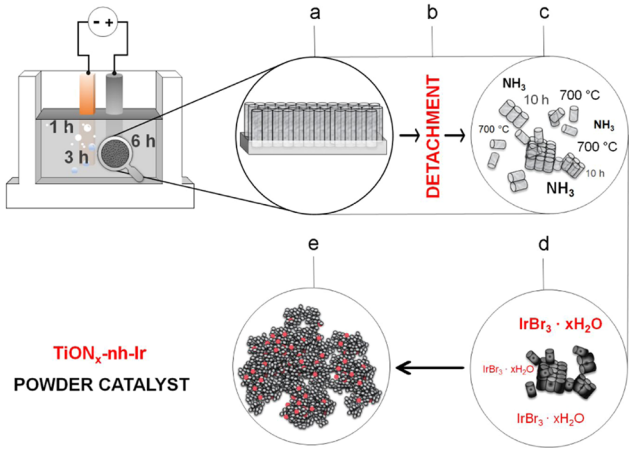

Figure 1. Procedure for $TiON_x$-*n*h-Ir catalyst preparation. (a) Anodic oxidation of titanium foil, (b) detachment of TiO_2 nanotubes, (c) annealing of detached TiO_2 nanotubes in ammonia, (d) deposition of Ir onto $TiON_x$ nanotubes, and (e) the final $TiON_x$-*n*h-Ir powder catalyst.

times were 1, 3, and 6 h. The amorphous TiO_2 nanotube film grown with anodic oxidation was washed with deionized water and ethanol. In the next step, TiO_2 nanotubes were simply detached from the metal titanium substrate by bending the anodized foil and thermally treating in ammonia at 700 °C for 10 h to convert the amorphous TiO_2 nanotubes into $TiON_x$. The flow of ammonia gas was kept constant at 50 cm^3 min^{-1}. After that, iridium nanoparticles on $TiON_x$ were prepared by dissolving 70 mg of iridium(III) bromide hydrate (Sigma-Aldrich, St. Louis, MO) in 1 mL of water at 50 °C. The solution was then mixed with 100 mg of $TiON_x$ powder (lightly milled in a mortar) at 50 °C until evaporation. Afterward, the mixture was thermally treated in a 5% H_2/Ar mixture. The temperature was increased at a rate of 2 °C min^{-1} to 450 °C for 1 h and then cooled to room temperature with a rate of 3 °C min^{-1}. After the thermal treatment, the final composite material contained 11 wt % iridium nanoparticles, as determined with inductively coupled plasma-optical emission spectroscopy (ICP-OES). The samples were denoted $TiON_x$-*n*h-Ir, where *n* can be 1, 3, or 6 and represents the anodization time.

2.2. Material Characterization. Scanning electron microscopy (SEM) was carried out using a Zeiss Supra 35 VP (Carl Zeiss, Oberkochen, Germany) microscope equipped with an energy-dispersive X-ray (EDX) spectrometer (Oxford Instruments, model Inca 400). The operating voltage was set to 7 kV. Detailed STEM analyses of the structural and elemental features of the samples were performed in a Cs-corrected transmission electron microscope (TEM, CF-ARM JEOL 200) equipped with an SSD JEOL EDX spectrometer and a GATAN Quantum ER dual-electron energy loss spectroscopy (EELS) spectrometer. An operating voltage of 80 kV was employed. XRD spectra of the samples were recorded on a flat, disclike, Si sample holder using an X-ray powder diffractometer PANalytical X'Pert PRO MPD (PANalytical B.V., Almelo, The Netherlands) with Cu $K_{\alpha 1}$ radiation having a wavelength of 1.5406 Å in the $\alpha 1$ configuration with a Johansson monochromator on the primary side. The diffractograms were recorded with 0.034° resolution and 100 s signal integration time in the 2θ range from 20 to 100°. Phases were identified with the X'Pert

https://dx.doi.org/10.1021/acscatal.0c04741
ACS Catal. 2021, 11, 670−681

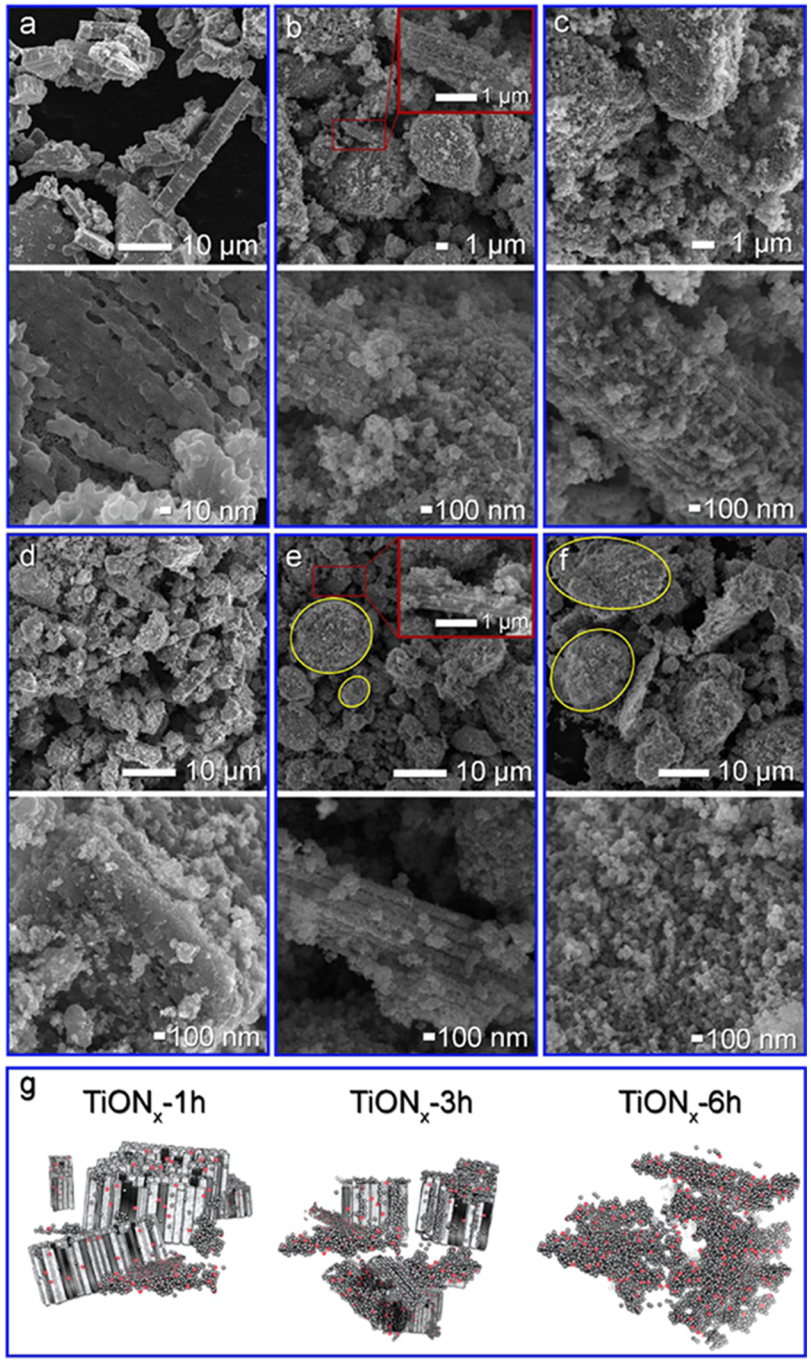

Figure 2. SEM micrographs of the synthesized catalysts: TiON$_x$-1h-Ir (a), TiON$_x$-3h-Ir (b), TiON$_x$-6h-Ir (c) and milled TiON$_x$-1h-Ir (d), TiON$_x$-3h-Ir (e), and TiON$_x$-6h-Ir (f). Inset figures (b) and (e) show the nanotubular morphology of the TiON$_x$-3h-Ir sample. A schematic presentation of all three milled catalysts is shown in (g).

HighScore Plus program using the International Centre for Diffraction Data (ICDD) PDF-4+ 2019 database.[33]

An inductively coupled plasma-optical emission spectrometry (ICP-OES) instrument (Varian 715-ES) was used to determine the iridium content in the samples.

The standards were prepared in-house by diluting traceable, certified, ICP-grade, single-element standards (Merck CertiPUR). The dilution of the samples and standards involved ultrapure water (Milli-Q, Millipore), HNO_3, and HCl (Merck, Suprapur). The samples were weighed and subsequently digested using a microwave-assisted digestion system (CEM MDS-2000) in 3/1 v/v HCl/HNO_3. The digested samples were then cooled to room temperature and diluted with 2% v/v HNO_3 until their concentration was in the desired range for ICP-OES measurements.

XPS was used to characterize the surface of the TiON$_x$-Ir catalysts (the upper 3−5 nm) using a PHI-TFA XPS spectrometer produced by Physical Electronics Inc. and equipped with an Al-monochromatic source. The analysis area was 0.4 mm in diameter, and two measurements were performed on every sample. The surface composition was calculated without taking into account any carbon, supposing that it originates from surface contamination.

https://dx.doi.org/10.1021/acscatal.0c04741
ACS Catal. 2021, 11, 670−681

The Ti K-edge absorption spectra of the $TiON_x$-3h-Ir and $TiON_x$-6h-Ir samples and the reference Ti compounds (TiO_2 anatase and rutile, and TiN) were measured at room temperature in the transmission detection mode using the X-ray absorption fine structure (XAFS) beamline of the ELETTRA synchrotron radiation facility in Trieste, Italy. The samples of powder mixed with carbon black were pressed into homogenous pellets having a total absorption thickness (μd) of about 2 above the Ti K-edge. A Si(111) double-crystal monochromator was used with an energy resolution of 0.5 eV at 5 keV. Higher-order harmonics were effectively eliminated by detuning the monochromator crystals to 60% of the rocking-curve maximum. The intensity of the monochromatic X-ray beam was measured using three consecutive 30-cm-long ionization detectors, filled with appropriate gas mixtures: 200 mbar N_2 and 1800 mbar He in the first, 1100 mbar N_2 and 900 mbar He in the second, and 140 mbar Ar, 1000 mbar N_2, and 600 mbar He in the third detector. The absorption spectra were measured in the interval from −250 to +1000 eV relative to the Ti K-edge. In the X-ray absorption near-edge structure (XANES) region, equidistant energy steps of 0.25 eV were used with an integration time of 1 s per step. Three repetitions of the scans were superimposed to improve the signal-to-noise ratio. The exact energy calibration was established with a simultaneous absorption measurement on a 5-μm-thick Ti metal foil placed between the second and third ionization chambers. The Ti K-edge in the Ti metal is at 4966 eV. The absolute energy reproducibility of the measured spectra was 0.03 eV. Data analyses of the X-ray absorption spectroscopy (XAS) spectra were performed with the Demeter (IFEFFIT) program package.[34]

The Brunauer−Emmett−Teller (BET) surface-area and nitrogen-sorption measurements for the samples were recorded using a Tristar 3000 automated gas-adsorption analyzer (Micromeritics Instrument Corp.) recording at −196 °C. Before the adsorption analysis, the samples were outgassed under vacuum for 12 h at 120 °C.

The Raman spectra were obtained on a confocal WITec Alpha 300 Raman spectrometer. The powdered samples were positioned on a silicon-wafer substrate under a green excitation-laser wavelength of 532 nm. The spectra were measured at four different positions using a 20× objective, an integration time of 1 s, and 100 scans. Four individual Raman spectra were recoded for each sample. The most representative spectrum for presentation was chosen by, first, omitting the most- and the least-intense spectra. From the remaining two, the spectrum approaching more closely the average values of all of the spectra was plotted. Due to the largest spreading of the intensity values, both middle spectra are shown as representative examples in the case of the $TiON_x$-6h-Ir sample.

2.3. Electrochemical Measurement. For the electrochemical measurements, each sample was dispersed in Milli-Q water (18.2 MΩ cm) to obtain a suspension with a final concentration of 1 mg_{cat} mL^{-1}. After sonication of the suspension, which ensured good homogeneity, a 20 μL droplet was cast-dropped on a 0.196 cm^2 glassy carbon working electrode embedded in a Teflon tip. We used a two-compartment, three-electrode setup. Pt wire and Ag/AgCl were used as the counter and reference electrodes, respectively. During the stability test, the Pt wire was replaced by a graphite rod to avoid any dissolution/redeposition of the Pt on the catalyst. The reference electrode was separated from the rest of the cell to avoid Cl^- contamination. An Ar-saturated $HClO_4$ 0.1 M (Merck, Suprapur, 70%) was used as an electrolyte. The potential was cycled between 0.05 and 1.6 V vs a reversible hydrogen electrode (RHE) at 1600 rpm and 20 mV s^{-1} until a stable cyclic voltammogram (CV) was obtained (less than 10 cycles). The last stable CV was used to estimate the activity. The potential was controlled with a potentiostat (potentiostat ECI-200, Nordic Electrochemistry). Prior to the experiment, the resistance of the solution was recorded by electrochemical impedance spectroscopy (EIS) and the *iR* was compensated accordingly during the activity measurement. The potentials are referred to the reversible hydrogen electrode (RHE), which was measured by saturating the electrolyte with hydrogen and measuring the open-circuit potential with a Pt black commercial catalyst on the working electrode. How to rigorously test the stability of OER catalysts is still the subject of discussion, as different protocols are employed.[15,35−38] Here, a chronopotentiometry test was performed as a preliminary stability test to simulate the operating potentials. A current of 1 mA mg_{Ir}^{-1} was applied to the catalyst for 1 and 2 h as suggested by Spöri et al.[39] Then, the electrolyte was replaced with a fresh solution to re-estimate the activity via a stable cyclic voltammogram (CV) at 1600 rpm and 20 mV s^{-1}.

3. RESULTS AND DISCUSSION

3.1. Characterization of $TiON_x$-*n*h-Ir Electrocatalysts. SEM, STEM, BET, XRD, XPS, and XAS at Ti K-edge and ICP-OES analyses were performed to fully characterize the synthesized electrocatalysts. As the morphology of the $TiON_x$ support has an important influence on the gas-evolving catalytic performance of the catalyst,[40] the influence of the anodization time during the first step of the synthesis process as well as the milling procedure in the last step of the synthesis was studied. A detailed description of the morphological changes during the starting phases of the synthesis process can be found in the Supporting Information (Section S1). As demonstrated by the thorough analysis of our samples, morphology is the only parameter we varied in our study.

The morphology of the prepared $TiON_x$-*n*h-Ir electrocatalysts is shown in Figure 2. The reason for the crushed nanotube arrays in all of the images is the wet impregnation technique, which included slight milling to obtain a homogeneous distribution of the iridium. Figure 2a−c shows as-prepared electrocatalysts, while Figure 2d−f shows the same samples after an additional, more rigorous, milling procedure. The final electrocatalysts presented in Figure 2d−f are schematically shown in Figure 2g. The milling procedure had the largest influence on the morphology of the $TiON_x$-Ir powders that were anodized for 3 and 6 h. The reason for this is the higher mechanical stability of the nanotube arrays prepared during 1 h of anodization, which is a consequence of the shorter length and thicker wall of these nanotubes. With a longer anodization time, the wall of the nanotubes at the top of the immobilized film becomes thinner (Figure S1), resulting in greater brittleness when applying physical force during milling. It can be observed that the sample anodized for 1 h (Figure 2a) consists of relatively large nanotube arrays, which become smaller after milling (Figure 2d). The morphology of the sample anodized for 3 h (Figure 2b) shows clusters with a nanotubular morphology, which can still be found after reducing the cluster size with milling (Figure 2e). In the sample anodized for 6 h, no nanotubular morphology features can be recognized anymore, even before the rigorous milling (Figure 2c). This is due to the formation of less mechanically

https://dx.doi.org/10.1021/acscatal.0c04741
ACS Catal. 2021, 11, 670−681

stable nanotubes during the excessive etching in the longest anodization process. However, the cluster size of the 6 h sample is the largest before and after the rigorous milling (Figure 2f). The average cluster size of the final electrocatalyst anodized for 3 h shown in Figure 2e is approximately 50 ± 3 μm, compared to approximately 121 ± 7 μm in the case of $TiON_x$-6h-Ir shown in Figure 2f. The main difference between the electrocatalysts prepared with anodic oxidation and other synthesis procedures is the defined orientation resembling the nanotubes. It should be noted that the time for the anodic oxidation should not be too long, as, in this case, the top surface starts losing the morphology of the nanotubes during anodization. If the anodization process is extended for even longer times, the nanotubes would start turning into nanoparticles with a morphology similar to that of an electrocatalyst prepared from commercial nanopowders (e.g., TiO_2 P25). The described loss of the nanotubular structure and the formation of nanoparticles occurred to some extent in the case of the $TiON_x$-6h sample and are shown in Figure S2c,d.

Additional morphological characterization of the samples was performed with STEM, and the average particle size of the iridium was determined. The average size of the iridium nanoparticles was, for all of the samples, between 3.1 and 3.4 nm, as seen in Table 1 and Figure S4. The iridium nanoparticles are evenly dispersed on the $TiON_x$ support, as seen for $TiON_x$-3h-Ir in Figure 3 and $TiON_x$-1h-Ir and $TiON_x$-6h-Ir in Figure S5.

Table 1. Average Particle Size as Determined by the STEM Image Analyses and the Amount of Nitrogen and Oxygen in the $TiON_x$ Support for the $TiON_x$-*n*h-Ir Samples, as Determined with EELS and XPS

	$TiON_x$-1h-Ir	$TiON_x$-3h-Ir	$TiON_x$-6h-Ir
average particle size (nm)	3.1 ± 1.0	3.3 ± 1.1	3.4 ± 1.1
number of particles	500	430	370
$TiON_x$ Support Composition (atom %) (Determined with EELS)			
N	20 ± 3	19 ± 5	22 ± 3
O	34 ± 4	34 ± 4	32 ± 3
O/N	1.71 ± 0.46	1.98 ± 0.77	1.5 ± 0.36
$TiON_x$ Support Composition (atom %) (Determined with XPS)			
N	13 ± 1.3	15.6 ± 1.6	13.2 ± 1.3
O	53.4 ± 5	51.6 ± 5	54.3 ± 5
O/N	4.11 ± 0.41	3.31 ± 0.33	4.11 ± 0.41

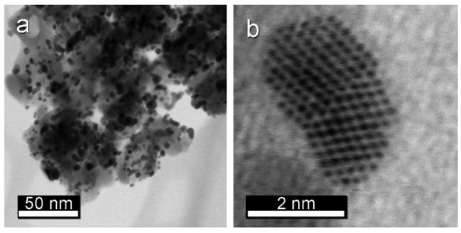

Figure 3. STEM images of $TiON_x$-3h-Ir showing well-dispersed Ir nanoparticles (a) and atomic-resolution image of an individual Ir nanoparticle (b).

The EELS and XPS results show that the compositions are very similar (Tables 1 and S1) for all three samples. As can be seen from the XPS results in Figure 4a, the surface concentrations of the titanium, oxygen, nitrogen, and iridium elements are independent of the anodization time. However, a

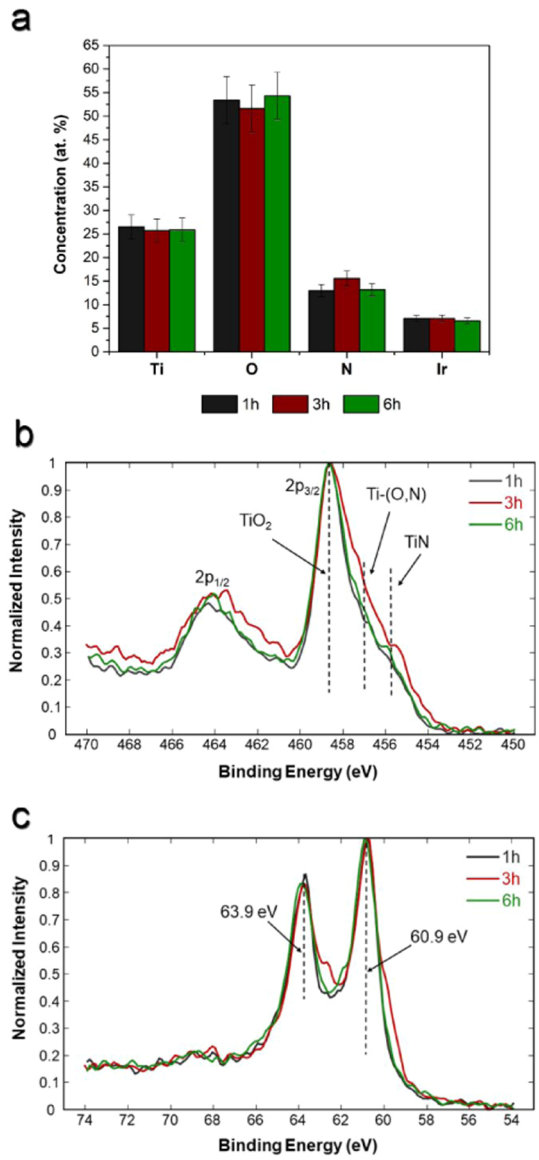

Figure 4. Surface composition in atom % determined with XPS on $TiON_x$-*n*h-Ir samples (a). Normalized XPS spectra of Ti 2p (b) and Ir 4f (c) of milled $TiON_x$-1h-Ir, $TiON_x$-3h-Ir, and $TiON_x$-6h-Ir.

difference in the O/N ratio determined with EELS (within the uncertainty of the measurement, the values are between 1.5 and 2) and XPS (within the uncertainty of the measurement, the values are between 3.3 and 4.1) can be observed (Table 1). The reason for this is the oxidation of the $TiON_x$ surface (upper 3−5 nm) that most likely occurred during milling. This is beneficial as it should protect the bulk material from further oxidation during the electrocatalytic experiments. The peaks observed in the Ti 2p XPS spectra (Figure 4b) are characteristic of TiO_2 (Ti^{4+} at 458.6 eV), Ti−ON (457.2 eV), and TiN (455.7 eV).[41] Some 65% of the titanium is in the TiO_2 state, while 20% is Ti−ON and 15% is TiN. The XPS spectra of Ir 4f (Figure 4c) are also similar for all of the samples. They mainly consist of peaks characteristic for iridium in the oxidation state zero (Ir^0 at 60.9 eV) with a possible minor portion of iridium in oxidation state 4 (Ir^{4+}) or 3 (Ir^{3+}).[42] The metallic state of iridium is expected from the synthesis procedure as no oxidation step was introduced; however, it changes with the electrochemical oxidation.

https://dx.doi.org/10.1021/acscatal.0c04741
ACS Catal. 2021, 11, 670−681

Independently, the presence of TiO_2 in the samples was also confirmed using Raman spectroscopy (Figure 5). The spectra

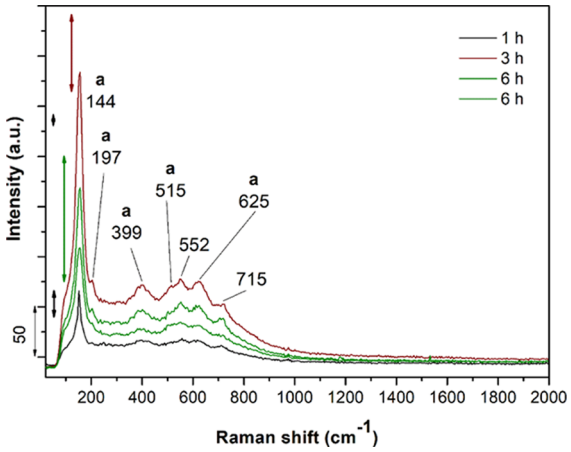

Figure 5. Raman spectra of $TiON_x$-*n*h-Ir powders. The representative spectra are shown, while all of the measurements are gathered in Figure S6 in the Supporting Information. Two representative spectra are presented for the $TiON_x$-6h-Ir sample due to the largest spread of the intensity values. The arrows denote the intensity ranges of the 144 cm^{-1} anatase bands detected for each type of sample.

reveal the presence of anatase[43] through the appearance of bands at 144 (E_g), 197 (E_g), 399 (B_{1g}), 515 (A_{1g}, B_{1g}), and 625 (E_g) cm^{-1}. However, the bands' intensities differ for the different samples (Figure 5) but also at various sites on the same sample (all four spectra recorded at various sites of each sample are shown in Figure S6 in the Supporting Information). The Raman spectra in Figure 5 were chosen as the most representative, with the arrows marking the measured range of the 144 cm^{-1} band intensities. The intensities are the highest and showed the smallest spread for the $TiON_x$-3h-Ir sample. This indicates the largest ordering with respect to the anatase phase. Three out of four spectra exhibited considerably lower intensities of anatase bands in $TiON_x$-1h-Ir (Figure S6), which reveals that the TiO_2 is closer to the amorphous state. The spectra of $TiON_x$-6h-Ir reveal the largest spread of the spectral intensities, indicating that the long-range ordering in anatase could be in any state between the 1 and 3 h samples.

The basis of the anatase bands increases with an increase in the band intensity. Such effects have already been ascribed to the nanometric size.[44] However, a debate has been going on about the possible presence of TiN or $TiON_x$ bands in this region. Namely, the Raman spectrum of TiN is characterized by a broad double band at 190−350 cm^{-1} and an additional one between 550 and 565 cm^{-1}.[45,46] The relative ratios among those bands change with the deficiencies in the nitrogen TiN_x.[47] The described TiN, TiN_x, and $TiON_x$ bands could be superimposed in the considered spectral range. For example, Prokes et al.[48] studied nitrided TiO_2 nanopowder. The authors suggested the presence of $TiO_{2-x}N_x$ due to the appearance of the shoulder band near 550 cm^{-1} in the Raman spectrum, dominated by the anatase bands. A similar assumption can be made for our $TiON_x$-*n*h-Ir samples since the band at 552 cm^{-1} can be observed in the spectra (Figures 5 and S6). XPS (Figure 4b) reveals the largest amount of Ti−(O,N) and TiN in the $TiON_x$-3h-Ir sample, which matches our results from Raman spectroscopy (Figures 5 and S6). The exact determination of the $TiON_x$, TiN bands and the solution to this dilemma demand a careful preparation of various standard compounds and a determination of their spectra, which will be addressed in our future work.

An interesting feature that also appears in the Raman spectra is a shoulder band at approximately 715 cm^{-1} (Figures 5 and S6). Such a band can confirm the presence of the Ir^{4+} state observed by XPS (Figure 4c). Specifically, we detected 541 and 712−717 cm^{-1} Raman bands for various commercial IrO_2 samples. The literature reports the appearance of IrO_2 at 561 and ∼720 cm^{-1} in chemical-vapor-deposited and sputtered samples.[49] The deviation from the bands of the IrO_2 single crystal (561 (E_g), 728 (B_{2g}), and 752 (A_{1g})), i.e., the red-shift of the bands' locations and asymmetric broadening, was ascribed to the nanometric size effects and residual stress effects. Consequently, 715 cm^{-1} could reflect the presence of oxidized Ir in the 4+ oxidation state. The second relevant band, i.e., 541 cm^{-1}, could be blurred by the presence of the 515 cm^{-1} band of anatase and the vibration at 552 cm^{-1}.

Ti K-edge X-ray absorption spectroscopy analysis (XANES and EXAFS) of the as-prepared and milled $TiON_x$-3h-Ir and $TiON_x$-6h-Ir was performed to compare the chemical state and local structure of the Ti cations in the samples (Figure S7a−c). The XANES results clearly show that the local structure, symmetry, and valence state of the Ti cations are the same in all of the samples. The anodic oxidation of the samples has no effect on the Ti chemical state in the sample, independent of the anodization time. We noted that the X-ray absorption spectroscopy analysis cannot distinguish the long-range ordering of the catalyst's surface, which Raman spectroscopy does. Therefore, these two characterization techniques are very complementary.

The total amount of Ir in the samples was measured by ICP-OES. This is crucial for determining the appropriate electrocatalytic activity, which was normalized to the mass of iridium in each sample. The amount of iridium in all of the samples was approximately 11 wt %. Again, the observed morphological differences due to the different anodization time did not influence the amount and size of the deposited iridium nanoparticles on the $TiON_x$ supports.

The chemical structures of all of the samples were determined with XRD analyses (Figures 6 and S7). Figure 6 shows the XRD spectra of the sample anodized for 3 h for all of the stages of its preparation. The TiO_2 nanotubes grown by anodic oxidation are amorphous and show no diffraction peaks (Figure 6, top). Annealing in ammonia at 700 °C transforms

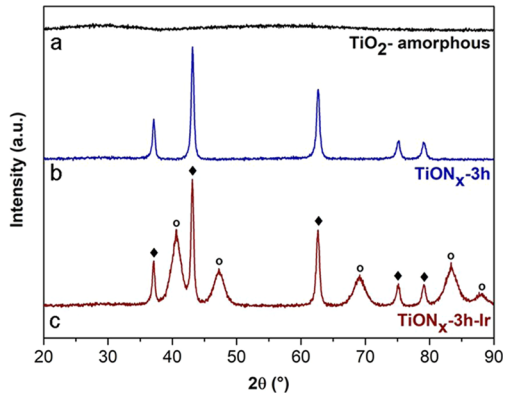

Figure 6. XRD spectra for amorphous TiO_2 (a), $TiON_x$-3h (b), and $TiON_x$-3h-Ir (c) samples.

https://dx.doi.org/10.1021/acscatal.0c04741
ACS Catal. 2021, 11, 670−681

the amorphous nanotubes into $TiON_x$ (Figure 6, middle). The diffraction peaks of $TiON_x$ are related to (♦) cubic titanium oxide nitride at 37.1° (111), 43.1° (200), 62.5° (220), 75.0° (311), and 94.4° (400) angles (PDF 01-084-4872).[33] The XRD spectrum of $TiON_x$-3h-Ir is shown at the bottom of Figure 6. The additional diffraction peaks are observed at 40.7° (111), 47.3° (200), 69.1° (220), 83.4° (311), and 88.1° (222) angles, corresponding to cubic Ir (○) (PDF 04-007-8342).[33] The comparison of the XRD spectra of all three $TiON_x$-*n*h and $TiON_x$-*n*h-Ir samples is shown in Figure S8 and reveals that the chemical structures of all of the $TiON_x$-*n*h and all of the $TiON_x$-*n*h-Ir are the same. The diffraction domains of the surface TiO_2 (for instance, anatase seen on $TiON_x$-3h) seen by Raman spectroscopy are obviously too small to sufficiently scatter the X-rays and be measured by our machine.

3.2. Electrochemical Activity of $TiON_x$-Ir. The electrochemical activity for the OER was determined for the case of several Ir-based analogues (Figure 7). The commercial catalyst,

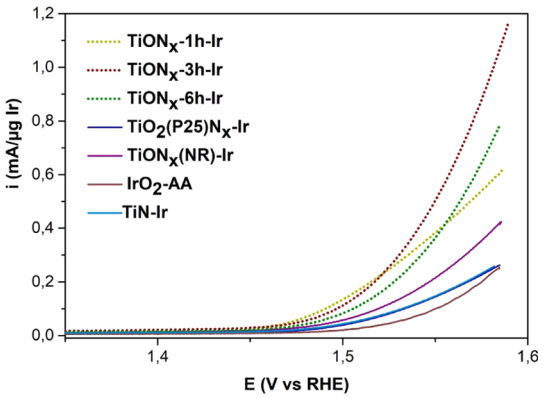

Figure 7. OER polarization curves. The curves were obtained at 20 mV s^{-1}, in 0.1 M $HClO_4$, 1600 rpm.

IrO_2 (Alfa Aesar), was chosen to represent the state of the art, while other homemade "benchmark catalysts" were synthesized to obtain Ir on TiN and Ir on $TiON_x$ supports. The latter two were prepared either from the commercial TiO_2 powder or from TiO_2 nanoribbons (see Section 2). The "benchmarks" were compared to the anodically grown analogues. This comparison is justified by the fact that such a selection makes possible an appropriate comparison of (i) the support type effect in terms of chemical composition as well as (ii) the potential effect of the morphology on OER's performance. In addition, a thorough comparison with Ir nanoparticles on Ti-based support from the literature can be difficult due to the differences in ink preparation, activation protocol, ionomer–catalyst ratio, or electrochemical conditions. However, the comparison of our samples with regard to the current literature can be found in Table S2.

The influence of the electrode morphology is clearly seen when the anodically grown catalysts are compared to the nonanodized analogues. Evidently, the anodically grown samples are superior for the entire OER region (Figure 7; see also Table 2). The comparison demonstrates an up to twofold-higher OER activity in the case of the anodically grown analogues (measured at 1.55 V, Table 2), which highlights the decisive role of the support morphology for the OER. More specifically, according to the structural analysis, the morphology of the $TiON_x$ support does not affect either the iridium deposition or the extent of the dispersion of the Ir

Table 2. Electrochemical Performances (Averaged over Three Measurements)

sample	mass activity at 1.55 V vs RHE (A g_{Ir}^{-1})	Tafel slope (mV dec^{-1})
$TiON_x$-1h-Ir	360.9 ± 18.7	±60
after degradation (2 h)	245.4 ± 12.8	±72
$TiON_x$-3h-Ir	520.3 ± 50.6	
after degradation (1 h)	405.8 ± 39.5	±63
after degradation (2 h)	385.0 ± 37.5	±77
$TiON_x$-6h-Ir	369.5 ± 35.1	±65
after degradation (2 h)	223.5 ± 21.2	±77
TiO_2(P25)N_x-Ir	143.9 ± 12.1	±71
TiNIr	147.5 ± 11.4	±75
IrO_2-AA	99.8 ± 14.3	±70
$TiON_x$(NR)-Ir	213.2 ± 26.9	±77

nanoparticles, i.e., a similar Ir particle size distribution is found for all anodically grown analogues (Figure S4). Additionally, even when the nanotube-array structure was reduced during mechanical grinding, the dispersion of iridium remained the same for all samples (Figures 3a and S5).

Within the family of anodically grown analogues, the following trend in the OER's performance is obtained. At low overpotentials (<1.52 V), the activity trend is in the following order: $TiON_x$-1h-Ir > $TiON_x$-3h-Ir > $TiON_x$-6h-Ir. However, at higher potentials (>1.52 V), this trend is altered: $TiON_x$-3h-Ir > $TiON_x$-6h-Ir > $TiON_x$-1h-Ir. To understand this better, it is important to note that the OER polarization curve consists of two regimes: (i) at lower potentials, the OER is governed by kinetics, which is influenced by the chemical structure of active sites,[50−52] their surface structure,[9,52,53] electronic interactions,[52,54] and interactions with the support;[15,55−58] while (ii) at higher potentials, the OER regime is controlled by electron transport and the transport/removal of the oxygen bubbles. The latter is caused due to confinement and results in the alternation of the local concentration of reactants or products. More specifically, it results in a decrease of local pH[59] or accumulation of evolved oxygen that can further lead to bubble formation. The gas-bubble effect not only limits the mass transport but also lowers the active surface area due to the generated O_2 gas. The latter blocks the active sites and thus hinders the access of water as a reactant. Hence, the effective detachment of gas bubbles is essential for an efficient reaction to proceed at high potentials. Notably, the frequency and critical bubble diameter of the detachment decisively depend on the electrode morphology.[60−66] The results presented here indicate that (i) in the kinetic regime (low potentials) the nanotube-array morphology (characteristic feature in $TiON_x$-1h-Ir) decisively promotes the OER, whereas during the transition to higher potentials a combination of cluster size and nanotubular morphology (characteristic feature in $TiON_x$-3h-Ir) decisively governs the reaction proceeding. The cluster size in particular should decisively impact the OER proceeding via bubble management (at higher potentials, i.e., higher reaction rates).[60−66] However, also $TiON_x$ particle-to-particle electron resistance through the oxidized surface contact points could lower the OER.[31,67] As

https://dx.doi.org/10.1021/acscatal.0c04741
ACS Catal. 2021, 11, 670−681

$TiON_x$-1h-Ir has the lowest number of them statistically, this could also explain its higher OER activity at the onset. This reasoning fits well when considering the case of $TiON_x$-6h-Ir. Its OER performance in the low-potential region is the least among the three analogues, which can be ascribed to the absence of a nanotubular morphology and the highest amount of contact points, whereas at the same time, a more promising OER performance is shown at higher potentials. It seems that $TiON_x$-3h-Ir has the best tradeoff between the electron and mass transport issues.

Note that based on the XPS, EELS, and Raman analyses, the surface of the support for all three analogues is rich in the TiO_2 phase (see discussion in Section 3.1). As shown before, TiO_2 can also induce passivation (besides $TiON_x$ particle-to-particle contact points), which influences the electron access for Ir nanoparticles, and hence the OER's kinetics.[68,69] To provide circumstantial evidence, we again rely on XPS and Raman analyses. Both techniques reveal the highest amount of the Ti−(O,N) phase to be present in the $TiON_x$-3h-Ir sample (Figures 4b, 5, and S6). This phase is important so as to retain sufficient electron conductivity for the OER (note that $TiON_x$ has significantly larger electronic conductivity than TiO_2 as directly shown in our recent study),[55] which is in agreement with the high catalytic activity of $TiON_x$-3h-Ir. Additionally, the Raman analysis reveals the different degrees of TiO_2 crystallinity, where the $TiON_x$-3h-Ir analogue has the most crystalline and $TiON_x$-1h-Ir has the most amorphous TiO_2 (Figure 5). We hypothesize that the differences in the crystallinity should be ascribed to the milling pretreatment. A correlation of the degree of TiO_2 crystallinity and the OER performance indicates that TiO_2 crystallinity could play an important role at higher OER potentials/current densities (Figure 7), which would be in line with the better electrochemical stability of the crystalline TiO_2 in comparison to the amorphous variant.[36,70−72] If not stabilized properly, the TiO_2 layer can become too thick for efficient electron conductance/tunneling.

To provide more insight, a Tafel analysis was performed. In the case of the anodically grown catalyst, similar Tafel slopes were found (60−65 mV dec^{-1}, Table 2). These values are comparable to the literature values for both the bulk, rutile IrO_2 and the electrochemically grown oxide.[15,73−75] Similar Tafel slopes indicate that the rate-determining step (RDS) is the same for all analogues within the family of anodically grown catalysts. In comparison, the Tafel slopes of nonanodically grown catalysts are higher (70−77 mV dec^{-1}, Table 2). Considering the small difference in the slope, we could reasonably expect that the RDS is the same for the two composite types compared here. Therefore, alternative reasoning is needed to explain the slope difference between the anodically grown and the nonanodized analogues. The literature data for similar systems[15,76,77] suggests that the Tafel slopes are changed due to the interaction between the Ir nanoparticles and the support. It has been shown previously that an unusually large Tafel slope can be associated with these interactions when using semiconducting catalytic materials such as TiO_2.[68,78] However, considering that both representatives of the $TiON_x$-based analogues (anodically grown and nonanodically grown) have the same chemical composition, we ascribe the steeper Tafel slope (the case of nonanodized samples) to the more extensive passive surface layer of TiO_2.[68,78] This reasoning is based on the Tafel slope's change after the electrochemical degradation (Table 2), where the Tafel slopes of anodically grown analogues increased to the values of the nonanodized samples (see discussion below). This is in line with the electrochemical oxidation of $TiON_x$ to TiO_2 during the degradation protocol.[68,69]

3.3. Electrochemical Stability of $TiON_x$-Ir. We noted that a standard OER benchmark degradation protocol is currently still lacking.[65] Different accelerated degradation tests (ADTs) have been used in the literature.[14,31−34] The most common ones are chronopotentiometry and potential cycling in the region of the OER potential (e.g., between 1 and 1.6 V vs RHE). The constant-current protocol was chosen as it is more destructive than the potentiodynamic treatment.[65] Apart from that, cycling to a potential higher than 1.6 V vs RHE can induce bubbles and block the surface of the catalyst, which can protect the catalyst from degradation, and thus lead to the wrong conclusions.[65,79] Longer stability tests can also be an issue for the backing electrode. Indeed, here, glassy carbon electrodes were used, which can undergo degradation after long exposures to the high potentials. Thus, other backing electrodes, such as Au or Pt, should be employed for longer degradation tests in the future.[30] Here, a preliminary degradation test was performed on the catalyst by applying a constant current of 1 mA mg_{Ir}^{-1} for 2 h. Electrochemical stability was investigated for the case of the three anodically grown catalysts. Our results show that the most stable catalyst is $TiON_x$-3h-Ir, which retained 74.3% of the initial activity after 2 h (Figure 8). Importantly, the majority of the performance

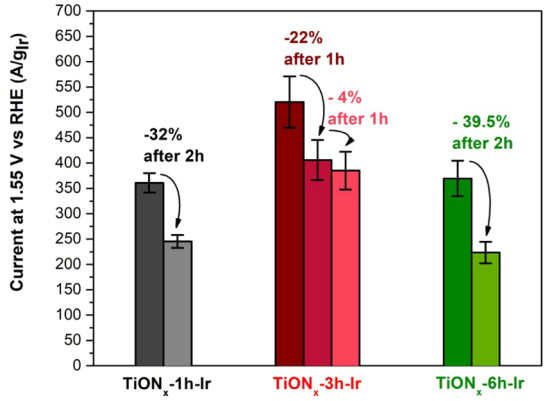

Figure 8. Activity remaining for the different samples after 2 h at 0.1 A mg_{Ir}^{-1}. $TiON_x$-1h-Ir in red, $TiON_x$-3h-Ir in blue, and $TiON_x$-6h-Ir in green.

loss occurs after half of galvanostatic perturbation; 78% of the initial activity is reached after 1 h (Figure 8). This suggests that catalyst-activity decay is slowing down, which means it could sustain the majority of the performance for an extended operating time. The activity loss could originate from (i) the dissolution of Ir nanoparticles, (ii) the physical detachment of Ir nanoparticles, or (iii) the electrochemical oxidation of $TiON_x$, leading to the formation of a passive nonconductive TiO_2 layer. However, according to a recent study, the effects of (i) and (ii) are not considered to play a significant role during degradation tests under ambient conditions and the timeframe of the thin-film rotating disk electrode (TF-RDE) setups.[65] Instead, we ascribe the activity loss to the influence of the electrochemical oxidation of the $TiON_x$ support, leading to the formation of TiO_2. This is supported by a slight increase in the Tafel slope after degradation perturbation (Table 2). Additionally, according to the OER's performance after the degradation protocol, we ascribe the performance−retention

https://dx.doi.org/10.1021/acscatal.0c04741
ACS Catal. 2021, 11, 670−681

trend to the different crystallinity degree of the surface TiO_2, where the $TiON_x$-3h-Ir analogue contains the most crystalline phase.[57] Even though additional dedicated studies are needed to investigate this effect further, it is reasonable to expect that the crystallinity of TiO_2 would play an important role, based on studies of oxide analogues.[36,70−72]

4. CONCLUSIONS

We have shown that Ir in the form of nanoparticles on a $TiON_x$ support made from anodically grown TiO_2 nanotubes exhibits a 5-times-better mass activity than commercial IrO_2 and at least 2-times-better mass activity than Ir on $TiON_x$ with different morphologies. Three different anodization times were investigated for the preparation of the TiO_2 nanotubes. The results for the OER's activity were in the order $TiON_x$-3h-Ir > $TiON_x$-6h-Ir ≥ $TiON_x$-1h-Ir. The better activity was assigned to the differences in the morphology of the support, as other properties like Ir particle size and metal loading were kept the same. Furthermore, the ratio between O/N was also similar in all of the samples, as determined by EDX, EELS, and XPS. The amount of iridium was approximately 11%, as measured by ICP-OES, and the average Ir particle size was 3.3 nm, as observed in STEM. The best stability was found for $TiON_x$-3h-Ir, which is promising as it is also the most active catalyst. We ascribed its superior performance to the nanotubular morphology and the presence of the anatase TiO_2 phase found on its surface by Raman spectroscopy. This anatase TiO_2 passivates and thus protects the $TiON_x$ surface and at the same induces beneficial effects on the Ir OER performance. In this way, we successfully synthesized an active and stable OER catalyst by supporting Ir nanoparticles on a $TiON_x$ support made from anodically grown TiO_2 nanotubes.

■ ASSOCIATED CONTENT

Supporting Information

The Supporting Information is available free of charge at https://pubs.acs.org/doi/10.1021/acscatal.0c04741.

Morphological changes during the synthesis process of all catalysts; iridium nanoparticles' size distribution; and composition, chemical structure, and Raman spectra of the prepared catalysts (PDF)

■ AUTHOR INFORMATION

Corresponding Authors

Primož Jovanovič − *Department of Materials Chemistry, National Institute of Chemistry, SI-1000 Ljubljana, Slovenia;* orcid.org/0000-0003-2477-3895; Email: primoz.jovanovic@ki.si

Nejc Hodnik − *Department of Materials Chemistry, National Institute of Chemistry, SI-1000 Ljubljana, Slovenia; Jožef Stefan International Postgraduate School, SI-1000 Ljubljana, Slovenia;* orcid.org/0000-0002-7113-9769; Email: nejc.hodnik@ki.si

Luka Suhadolnik − *Department for Nanostructured Materials, Jožef Stefan Institute, SI-1000 Ljubljana, Slovenia;* orcid.org/0000-0002-9103-6687; Email: luka.suhadolnik@ijs.si

Authors

Leonard Moriau − *Department of Materials Chemistry, National Institute of Chemistry, SI-1000 Ljubljana, Slovenia; Jožef Stefan International Postgraduate School, SI-1000 Ljubljana, Slovenia*

Marjan Bele − *Department of Materials Chemistry, National Institute of Chemistry, SI-1000 Ljubljana, Slovenia*

Živa Marinko − *Jožef Stefan International Postgraduate School, SI-1000 Ljubljana, Slovenia; Department for Nanostructured Materials, Jožef Stefan Institute, SI-1000 Ljubljana, Slovenia;* orcid.org/0000-0002-6054-8137

Francisco Ruiz-Zepeda − *Department of Materials Chemistry, National Institute of Chemistry, SI-1000 Ljubljana, Slovenia*

Gorazd Koderman Podboršek − *Department of Materials Chemistry, National Institute of Chemistry, SI-1000 Ljubljana, Slovenia; Jožef Stefan International Postgraduate School, SI-1000 Ljubljana, Slovenia*

Martin Šala − *Department of Analytical Chemistry, National Institute of Chemistry, SI-1000 Ljubljana, Slovenia;* orcid.org/0000-0001-7845-860X

Angelja Kjara Šurca − *Department of Materials Chemistry, National Institute of Chemistry, SI-1000 Ljubljana, Slovenia;* orcid.org/0000-0001-5339-4937

Janez Kovač − *Department of Surface Engineering, Jožef Stefan Institute, SI-1000 Ljubljana, Slovenia*

Iztok Arčon − *Laboratory of Quantum Optics, University of Nova Gorica, SI-5000 Nova Gorica, Slovenia; Department of Medium and Low Energy Physics, Jožef Stefan Institute, SI-1000 Ljubljana, Slovenia*

Complete contact information is available at: https://pubs.acs.org/10.1021/acscatal.0c04741

Notes

The authors declare no competing financial interest.

■ ACKNOWLEDGMENTS

The provision of financial support for the research and the preparation of the manuscript by the Slovenian Research Agency (ARRS) within the research programs P2-0084, P2-0393, P1-0034, and P1-0112 and project N2-0106 are gratefully acknowledged. P.J. acknowledges the financial support from the Slovenian Research Agency under the project Z1-9165. N.H. acknowledges funding from the European Research Council (ERC) under the European Union's Horizon 2020 research (Grant agreement ID: 852208). The access to synchrotron radiation facilities (XAFS beamline, projects 20185165 and 20175158) of ELETTRA is acknowledged as well as the support by the project CALIPSOplus under Grant Agreement 730872 from the EU Framework Programme for Research and Innovation HORIZON 2020 for the XAS experiment at Elettra. We thank Giuliana Aquilanti, Simone Pollastri, and Mateusz Czyzycki from the XAFS beamline for their assistance during the experiments and their expert advice on beamline operation. The authors also thank Edi Kranjc for the X-ray powder-diffraction measurements and Mojca Opresnik for the nitrogen-physisorption measurements (Department of Inorganic Chemistry and Technology, National Institute of Chemistry, Slovenia).

■ REFERENCES

(1) Katsounaros, I.; Cherevko, S.; Zeradjanin, A. R.; Mayrhofer, K. J. J. Oxygen Electrochemistry as a Cornerstone for Sustainable Energy Conversion. *Angew. Chem., Int. Ed.* **2014**, 102−121.

(2) Suen, N.-T.; Hung, S.-F.; Quan, Q.; Zhang, N.; Xu, Y.-J.; Chen, H. M. Electrocatalysis for the Oxygen Evolution Reaction: Recent

Development and Future Perspectives. *Chem. Soc. Rev.* **2017**, *46*, 337−365.
(3) Geiger, S.; Kasian, O.; Shrestha, B. R.; Mingers, A. M.; Mayrhofer, K. J. J.; Cherevko, S. Activity and Stability of Electrochemically and Thermally Treated Iridium for the Oxygen Evolution Reaction. *J. Electrochem. Soc.* **2016**, *163*, F3132−F3138.
(4) Ledendecker, M.; Geiger, S.; Hengge, K.; Lim, J.; Cherevko, S.; Mingers, A. M.; Göhl, D.; Fortunato, G. V.; Jalalpoor, D.; Schüth, F.; Scheu, C.; Mayrhofer, K. J. J. Towards Maximized Utilization of Iridium for the Acidic Oxygen Evolution Reaction. *Nano Res.* **2019**, *12*, 2275−2280.
(5) Faisal, F.; Stumm, C.; Bertram, M.; Waidhas, F.; Lykhach, Y.; Cherevko, S.; Xiang, F.; Ammon, M.; Vorokhta, M.; Šmíd, B.; Skála, T.; Tsud, N.; Neitzel, A.; Beranová, K.; Prince, K. C.; Geiger, S.; Kasian, O.; Wähler, T.; Schuster, R.; Schneider, M. A.; Matolín, V.; Mayrhofer, K. J. J.; Brummel, O.; Libuda, J. Electrifying Model Catalysts for Understanding Electrocatalytic Reactions in Liquid Electrolytes. *Nat. Mater.* **2018**, *17*, 592−598.
(6) Ding, Z.; Cheng, Q.; Zou, L.; Fang, J.; Zou, Z.; Yang, H. Controllable Synthesis of Titanium Nitride Nanotubes by Coaxial Electrospinning and Their Application as a Durable Support for Oxygen Reduction Reaction Electrocatalysts. *Chem. Commun.* **2017**, *53*, 13233−13236.
(7) Yu, X.; Hua, T.; Liu, X.; Yan, Z.; Xu, P.; Du, P. Nickel-Based Thin Film on Multiwalled Carbon Nanotubes as an Efficient Bifunctional Electrocatalyst for Water Splitting. *ACS Appl. Mater. Interfaces* **2014**, *6*, 15395−15402.
(8) Gong, M.; Li, Y.; Wang, H.; Liang, Y.; Wu, J. Z.; Zhou, J.; Wang, J.; Regier, T.; Wei, F.; Dai, H. An Advanced Ni−Fe Layered Double Hydroxide Electrocatalyst for Water Oxidation. *J. Am. Chem. Soc.* **2013**, *135*, 8452−8455.
(9) Reier, T.; Oezaslan, M.; Strasser, P. Electrocatalytic Oxygen Evolution Reaction (OER) on Ru, Ir, and Pt Catalysts: A Comparative Study of Nanoparticles and Bulk Materials. *ACS Catal.* **2012**, *2*, 1765−1772.
(10) Wang, L.; Song, F.; Ozouf, G.; Geiger, D.; Morawietz, T.; Handl, M.; Gazdzicki, P.; Beauger, C.; Kaiser, U.; Hiesgen, R.; et al. Improving the Activity and Stability of Ir Catalysts for PEM Electrolyzer Anodes by SnO 2:Sb Aerogel Supports: Does V Addition Play an Active Role in Electrocatalysis? *J. Mater. Chem. A* **2017**, *5*, 3172−3178.
(11) Han, B.; Risch, M.; Belden, S.; Lee, S.; Bayer, D.; Mutoro, E.; Shao-Horn, Y. Screening Oxide Support Materials for OER Catalysts in Acid. *J. Electrochem. Soc.* **2018**, *165*, F813−F820.
(12) Cheng, J.; Yang, J.; Kitano, S.; Juhasz, G.; Higashi, M.; Sadakiyo, M.; Kato, K.; Yoshioka, S.; Sugiyama, T.; Yamauchi, M.; Nakashima, N. Impact of Ir-Valence Control and Surface Nanostructure on Oxygen Evolution Reaction over a Highly Efficient Ir−TiO 2 Nanorod Catalyst. *ACS Catal.* **2019**, *9*, 6974−6986.
(13) Yi, Y.; Weinberg, G.; Prenzel, M.; Greiner, M.; Heumann, S.; Becker, S.; Schlögl, R. Electrochemical Corrosion of a Glassy Carbon Electrode. *Catal. Today* **2017**, *295*, 32−40.
(14) Silva, G. C.; Venturini, S. I.; Zhang, S.; Löffler, M.; Scheu, C.; Mayrhofer, K. J. J.; Ticianelli, E. A.; Cherevko, S. Oxygen Evolution Reaction on Tin Oxides Supported Iridium Catalysts: Do We Need Dopants? *ChemElectroChem* **2020**, *7*, 2330−2339.
(15) Oh, H.-S.; Nong, H. N.; Reier, T.; Bergmann, A.; Gliech, M.; Ferreira de Araújo, J.; Willinger, E.; Schlögl, R.; Teschner, D.; Strasser, P. Electrochemical Catalyst−Support Effects and Their Stabilizing Role for IrO x Nanoparticle Catalysts during the Oxygen Evolution Reaction. *J. Am. Chem. Soc.* **2016**, *138*, 12552−12563.
(16) Schalenbach, M. A Perspective on Low-Temperature Water Electrolysis − Challenges in Alkaline and Acidic Technology. *Int. J. Electrochem. Sci.* **2018**, *13*, 1173−1226.
(17) Suhadolnik, L.; Lašič Jurković, D.; Likozar, B.; Bele, M.; Drev, S.; Čeh, M. Structured Titanium Oxynitride (TiOxNy) Nanotube Arrays for a Continuous Electrocatalytic Phenol-Degradation Process: Synthesis, Characterization, Mechanisms and the Chemical Reaction Micro-Kinetics. *Appl. Catal., B* **2019**, *257*, No. 117894.
(18) Trenczek-Zajac, A.; Radecka, M.; Zakrzewska, K.; Brudnik, A.; Kusior, E.; Bourgeois, S.; Marco De Lucas, M. C.; Imhoff, L. Structural and Electrical Properties of Magnetron Sputtered Ti(ON) Thin Films: The Case of TiN Doped in Situ with Oxygen. *J. Power Sources* **2009**, *194*, 93−103.
(19) Sluban, M.; Umek, P.; Jagličić, Z.; Buh, J.; Šmitek, P.; Mrzel, A.; Bittencourt, C.; Guttmann, P.; Delville, M.-H.; Mihailović, D.; Arčon, D. Controlling Disorder and Superconductivity in Titanium Oxynitride Nanoribbons with Anion Exchange. *ACS Nano* **2015**, *9*, 10133−10141.
(20) Soliman, K. A.; Zedan, A. F.; Khalifa, A.; El-Sayed, H. A.; Aljaber, A. S.; AlQaradawi, S. Y.; Allam, N. K. Silver Nanoparticles-Decorated Titanium Oxynitride Nanotube Arrays for Enhanced Solar Fuel Generation. *Sci. Rep.* **2017**, *7*, No. 1913.
(21) Yan, L.; Chen, G.; Tan, S.; Zhou, M.; Zou, G.; Deng, S.; Smirnov, S.; Luo, H. Titanium Oxynitride Nanoparticles Anchored on Carbon Nanotubes as Energy Storage Materials. *ACS Appl. Mater. Interfaces* **2015**, *7*, 24212−24217.
(22) El-Hossary, F. M.; Negm, N. Z.; Abd El-Rahman, A. M.; Raaif, M.; Abd Elmula, A. A. Properties of Titanium Oxynitride Prepared by RF Plasma. *Adv. Chem. Eng. Sci.* **2015**, *05*, 1−14.
(23) Yang, H.; McCormick, P. G. Synthesis of Titanium Oxynitride by Mechanical Milling. *J. Mater. Sci.* **1993**, *28*, 5663−5667.
(24) Song, X.; Gopireddy, D.; Takoudis, C. G. Characterization of Titanium Oxynitride Films Deposited by Low Pressure Chemical Vapor Deposition Using Amide Ti Precursor. *Thin Solid Films* **2008**, *516*, 6330−6335.
(25) Zukalova, M.; Prochazka, J.; Bastl, Z.; Duchoslav, J.; Rubacek, L.; Havlicek, D.; Kavan, L. Facile Conversion of Electrospun TiO $_2$ into Titanium Nitride/Oxynitride Fibers. *Chem. Mater.* **2010**, *22*, 4045−4055.
(26) Roy, P.; Berger, S.; Schmuki, P. TiO_2 Nanotubes: Synthesis and Applications. *Angew. Chem., Int. Ed.* **2011**, *50*, 2904−2939.
(27) Suhadolnik, L.; Pohar, A.; Likozar, B.; Čeh, M. Mechanism and Kinetics of Phenol Photocatalytic, Electrocatalytic and Photoelectrocatalytic Degradation in a TiO_2-Nanotube Fixed-Bed Microreactor. *Chem. Eng. J.* **2016**, *303*, 292.
(28) Liu, G.; Wang, K.; Hoivik, N.; Jakobsen, H. Progress on Free-Standing and Flow-through TiO2 Nanotube Membranes. *Sol. Energy Mater. Sol. Cells* **2012**, *98*, 24−38.
(29) Lin, J.; Liu, X.; Zhu, S.; Liu, Y.; Chen, X. Anatase TiO_2 Nanotube Powder Film with High Crystallinity for Enhanced Photocatalytic Performance. *Nanoscale Res. Lett.* **2015**, *10*, No. 110.
(30) Lončar, A.; Moriau, L.; Stojanovski, K.; Ruiz-Zepeda, F.; Jovanovic, P.; Bele, M.; Gaberscek, M.; Hodnik, N. Ir/TiONx/C High-Performance Oxygen Evolution Reaction Nanocomposite Electrocatalysts in Acidic Media: Synthesis, Characterization and Electrochemical Benchmarking Protocol. *J. Phys. Energy* **2020**, No. 02LT01.
(31) Bele, M.; Stojanovski, K.; Jovanovič, P.; Moriau, L.; Koderman Podboršek, G.; Moškon, J.; Umek, P.; Sluban, M.; Dražič, G.; Hodnik, N.; Gaberščček, M. Towards Stable and Conductive Titanium Oxynitride High-Surface-Area Support for Iridium Nanoparticles as Oxygen Evolution Reaction Electrocatalyst. *ChemCatChem* **2019**, *11*, 5038−5044.
(32) Bele, M.; Jovanovič, P.; Marinko, Ž.; Drev, S.; Simon Šelih, V.; Kovač, J.; Gaberščček, M.; Koderman Podboršek, G.; Dražić, G.; Hodnik, N.; Kokalj, A.; Suhadolnik, L. Increasing the Oxygen-Evolution Reaction Performance of Nanotubular Titanium Oxynitride-Supported Ir Nanoparticles by a Strong Metal−Support Interaction. *ACS Catal.* **2020**, 13688−13700.
(33) Kabekkodu, S. N. *PDF-4+*; International Centre for Diffraction Data: Newton Square, PA, 2016.
(34) Ravel, B.; Newville, M. ATHENA, ARTEMIS, HEPHAESTUS: Data Analysis for X-ray Absorption Spectroscopy Using IFEFFIT. *J. Synchrotron Radiat.* **2005**, *12*, 537−541.
(35) Mccrory, C. C. L.; Jung, S.; Peters, J. C.; Jaramillo, T. F. Benchmarking Heterogeneous Electrocatalysts for the Oxygen Evolution Reaction. *J. Am. Chem. Soc.* **2013**, *135*, 16977−16987.

https://dx.doi.org/10.1021/acscatal.0c04741
ACS Catal. 2021, 11, 670−681

(36) Jovanovič, P.; Hodnik, N.; Ruiz-Zepeda, F.; Arčon, I.; Jozinović, B.; Zorko, M.; Bele, M.; Šala, M.; Šelih, V. S.; Hočevar, S.; Gaberščček, M. Electrochemical Dissolution of Iridium and Iridium Oxide Particles in Acidic Media: Transmission Electron Microscopy, Electrochemical Flow Cell Coupled to Inductively Coupled Plasma Mass Spectrometry, and X-Ray Absorption Spectroscopy Study. *J. Am. Chem. Soc.* **2017**, *139*, 12837−12846.
(37) Cherevko, S.; Reier, T.; Zeradjanin, A. R.; Pawolek, Z.; Strasser, P.; Mayrhofer, K. J. J. Stability of Nanostructured Iridium Oxide Electrocatalysts during Oxygen Evolution Reaction in Acidic Environment. *Electrochem. Commun.* **2014**, *48*, 81−85.
(38) Alia, S. M.; Rasimick, B.; Ngo, C.; Neyerlin, K. C.; Kocha, S. S.; Pylypenko, S.; Xu, H.; Pivovar, B. S. Activity and Durability of Iridium Nanoparticles in the Oxygen Evolution Reaction. *J. Electrochem. Soc.* **2016**, *163*, F3105−F3112.
(39) Spöri, C.; Kwan, J. T. H.; Bonakdarpour, A.; Wilkinson, D. P.; Strasser, P. The Stability Challenges of Oxygen Evolving Catalysts: Towards a Common Fundamental Understanding and Mitigation of Catalyst Degradation. *Angew. Chem., Int. Ed.* **2017**, 5994−6021.
(40) Zeradjanin, A. R. Frequent Pitfalls in the Characterization of Electrodes Designed for Electrochemical Energy Conversion and Storage. *ChemSusChem* **2018**, *11*, 1278−1284.
(41) Han, J. H.; Bang, J. H. A Hollow Titanium Oxynitride Nanorod Array as an Electrode Substrate Prepared by the Hot Ammonia-Induced Kirkendall Effect. *J. Mater. Chem. A* **2014**, *2*, 10568−10576.
(42) Pfeifer, V.; Jones, T. E.; Velasco Vélez, J. J.; Massué, C.; Arrigo, R.; Teschner, D.; Girgsdies, F.; Scherzer, M.; Greiner, M. T.; Allan, J.; Hashagen, M.; Weinberg, G.; Piccinin, S.; Hävecker, M.; Knop-Gericke, A.; Schlögl, R. The Electronic Structure of Iridium and Its Oxides. *Surf. Interface Anal.* **2016**, *48*, 261−273.
(43) Ohsaka, T.; Izumi, F.; Fujiki, Y. Raman Spectrum of Anatase, TiO2. *J. Raman Spectrosc.* **1978**, *7*, 321−324.
(44) Kontos, A. I.; Kontos, A. G.; Raptis, Y. S.; Falaras, P. Nitrogen Modified Nanostructured Titania: Electronic, Structural and Visible-Light Photocatalytic Properties. *Phys. Status Solidi RRL* **2008**, *2*, 83−85.
(45) György, E.; Pérez Del Pino, A.; Serra, P.; Morenza, J. L. Surface Nitridation of Titanium by Pulsed Nd:YAG Laser Irradiation. *Appl. Surf. Sci.* **2002**, *186*, 130−134.
(46) Ding, Z. H.; Yao, B.; Qiu, L. X.; Lv, T. Q. Raman Scattering Investigation of Nanocrystalline δ-TiNx Synthesized by Solid-State Reaction. *J. Alloys Compd.* **2006**, *421*, 247−251.
(47) Spengler, W.; Kaiser, R.; Christensen, A. N.; Müller-Vogt, G. Raman Scattering, Superconductivity, and Phonon Density of States of Stoichiometric and Nonstoichiometric TiN. *Phys. Rev. B* **1978**, *17*, 1095−1101.
(48) Prokes, S. M.; Gole, J. L.; Chen, X.; Burda, C.; Carlos, W. E. Defect-Related Optical Behavior in Surface-Modified TiO2 Nanostructures. *Adv. Funct. Mater.* **2005**, *15*, 161−167.
(49) Korotcov, A. V.; Huang, Y. S.; Tsai, D. S.; Tiong, K. K. Raman Scattering Characterization of Vertical Aligned 1D IrO2 Nanocrystals Grown on Single Crystal Oxide Substrates. *Solid State Commun.* **2006**, *137*, 310−314.
(50) Kim, Y. T.; Lopes, P. P.; Park, S. A.; Lee, A. Y.; Lim, J.; Lee, H.; Back, S.; Jung, Y.; Danilovic, N.; Stamenkovic, V.; Erlebacher, J.; Snyder, J.; Markovic, N. M. Balancing Activity, Stability and Conductivity of Nanoporous Core-Shell Iridium/Iridium Oxide Oxygen Evolution Catalysts. *Nat. Commun.* **2017**, *8*, No. 1449.
(51) Seitz, L. C.; Dickens, C. F.; Nishio, K.; Hikita, Y.; Montoya, J.; Doyle, A.; Kirk, C.; Vojvodic, A.; Hwang, H. Y.; Norskov, J. K.; Jaramillo, T. F. A Highly Active and Stable IrO x /SrIrO 3 Catalyst for the Oxygen Evolution Reaction. *Science* **2016**, *353*, 1011−1014.
(52) Chang, S. H.; Danilovic, N.; Chang, K.-C.; Subbaraman, R.; Paulikas, A. P.; Fong, D. D.; Highland, M. J.; Baldo, P. M.; Stamenkovic, V. R.; Freeland, J. W.; Eastman, J. A.; Markovic, N. M. Functional Links between Stability and Reactivity of Strontium Ruthenate Single Crystals during Oxygen Evolution. *Nat. Commun.* **2014**, *5*, No. 4191.
(53) Chang, S. H.; Connell, J. G.; Danilovic, N.; Subbaraman, R.; Chang, K.-C.; Stamenkovic, V. R.; Markovic, N. M. Activity−Stability Relationship in the Surface Electrochemistry of the Oxygen Evolution Reaction. *Faraday Discuss.* **2014**, *176*, 125−133.
(54) Nong, H. N.; Reier, T.; Oh, H. S.; Gliech, M.; Paciok, P.; Vu, T. H. T.; Teschner, D.; Heggen, M.; Petkov, V.; Schlögl, R.; Jones, T.; Strasser, P. A Unique Oxygen Ligand Environment Facilitates Water Oxidation in Hole-Doped IrNiOx Core−Shell Electrocatalysts. *Nat. Catal.* **2018**, *1*, 841−851.
(55) Bele, M.; Stojanovski, K.; Jovanovič, P.; Moriau, L.; Koderman Podboršek, G.; Moškon, J.; Umek, P.; Sluban, M.; Dražič, G.; Hodnik, N.; Gaberščček, M. Towards Stable and Conductive Titanium Oxynitride High-Surface-Area Support for Iridium Nanoparticles as Oxygen Evolution Reaction Electrocatalyst. *ChemCatChem* **2019**, *11*, 5038−5044.
(56) Saveleva, V. A.; Wang, L.; Kasian, O.; Batuk, M.; Hadermann, J.; Gallet, J. J.; Bournel, F.; Alonso-Vante, N.; Ozouf, G.; Beauger, C.; Mayrhofer, K. J. J.; Cherevko, S.; Gago, A. S.; Friedrich, K. A.; Zafeiratos, S.; Savinova, E. R. Insight into the Mechanisms of High Activity and Stability of Iridium Supported on Antimony-Doped Tin Oxide Aerogel for Anodes of Proton Exchange Membrane Water Electrolyzers. *ACS Catal.* **2020**, *10*, 2508−2516.
(57) Kasian, O.; Li, T.; Mingers, A. M.; Schweinar, K.; Savan, A.; Ludwig, A.; Mayrhofer, K. J. J. Stabilization of an Iridium Oxygen Evolution Catalyst by Titanium Oxides. *J. Phys.: Energy* **2020**, 2515.
(58) Li, G.; Li, K.; Yang, L.; Chang, J.; Ma, R.; Wu, Z.; Ge, J.; Liu, C.; Xing, W. Boosted Performance of Ir Species by Employing TiN as the Support toward Oxygen Evolution Reaction. *ACS Appl. Mater. Interfaces* **2018**, *10*, 38117−38124.
(59) Katsounaros, I.; Meier, J. C.; Klemm, S. O.; Topalov, A. A.; Biedermann, P. U.; Auinger, M.; Mayrhofer, K. J. J. The Effective Surface PH during Reactions at the Solid-Liquid Interface. *Electrochem. commun.* **2011**, *13*, 634−637.
(60) Zeradjanin, A. R.; La Mantia, F.; Masa, J.; Schuhmann, W. Utilization of the Catalyst Layer of Dimensionally Stable Anodes—Interplay of Morphology and Active Surface Area. *Electrochim. Acta* **2012**, *82*, 408−414.
(61) Zeradjanin, A. R.; Topalov, A. A.; Van Overmeere, Q.; Cherevko, S.; Chen, X.; Ventosa, E.; Schuhmann, W.; Mayrhofer, K. J. J. Rational Design of the Electrode Morphology for Oxygen Evolution-Enhancing the Performance for Catalytic Water Oxidation. *RSC Adv.* **2014**, *4*, 9579−9587.
(62) Trieu, V.; Schley, B.; Natter, H.; Kintrup, J.; Bulan, A.; Hempelmann, R. RuO2-Based Anodes with Tailored Surface Morphology for Improved Chlorine Electro-Activity. *Electrochim. Acta* **2012**, *78*, 188−194.
(63) Zeradjanin, A. R.; Ventosa, E.; Bondarenko, A. S.; Schuhmann, W. Evaluation of the Catalytic Performance of Gas-Evolving Electrodes Using Local Electrochemical Noise Measurements. *ChemSusChem* **2012**, 1905.
(64) Chen, X.; Maljusch, A.; Rincón, R. A.; Battistel, A.; Bandarenka, A. S.; Schuhmann, W. Local Visualization of Catalytic Activity at Gas Evolving Electrodes Using Frequency-Dependent Scanning Electrochemical Microscopy. *Chem. Commun.* **2014**, *50*, 13250−13253.
(65) El-Sayed, H. A.; Weiß, A.; Olbrich, L. F.; Putro, G. P.; Gasteiger, H. A. OER Catalyst Stability Investigation Using RDE Technique: A Stability Measure or an Artifact? *J. Electrochem. Soc.* **2019**, *166*, F458−F464.
(66) Ohno, H.; Nohara, S.; Kakinuma, K.; Uchida, M.; Miyake, A.; Deki, S.; Uchida, H. Remarkable Mass Activities for the Oxygen Evolution Reaction at Iridium Oxide Nanocatalysts Dispersed on Tin Oxides for Polymer Electrolyte Membrane Water Electrolysis. *J. Electrochem. Soc.* **2017**, *164*, F944−F947.
(67) Hegge, F.; Lombeck, F.; Cruz Ortiz, E.; Bohn, L.; von Holst, M.; Kroschel, M.; Hübner, J.; Breitwieser, M.; Strasser, P.; Vierrath, S. Efficient and Stable Low Iridium Loaded Anodes for PEM Water Electrolysis Made Possible by Nanofiber Interlayers. *ACS Appl. Energy Mater.* **2020**, *3*, 8276−8284.

(68) Scheuermann, A. G.; Prange, J. D.; Gunji, M.; Chidsey, C. E. D.; McIntyre, P. C. Effects of Catalyst Material and Atomic Layer Deposited TiO2 Oxide Thickness on the Water Oxidation Performance of Metal-Insulator-Silicon Anodes. *Energy Environ. Sci.* **2013**, *6*, 2487−2496.
(69) Gebauer, C.; Fischer, P.; Wassner, M.; Diemant, T.; Jusys, Z.; Hüsing, N.; Behm, R. J. Performance of Titanium Oxynitrides in the Electrocatalytic Oxygen Evolution Reaction. *Nano Energy* **2016**, *29*, 136−148.
(70) Geiger, S.; Kasian, O.; Shrestha, B. R.; Mingers, A. M.; Mayrhofer, K. J. J.; Cherevko, S. Activity and Stability of Electrochemically and Thermally Treated Iridium for the Oxygen Evolution Reaction. *J. Electrochem. Soc.* **2016**, *163*, F3132−F3138.
(71) Hodnik, N.; Jovanovič, P.; Pavlišič, A.; Jozinović, B.; Zorko, M.; Bele, M.; Šelih, V. S.; Šala, M.; Hočevar, S.; Gaberšček, M. New Insights into Corrosion of Ruthenium and Ruthenium Oxide Nanoparticles in Acidic Media. *J. Phys. Chem. C* **2015**, *119*, 10140−10147.
(72) Schweinar, K.; Gault, B.; Mouton, I.; Kasian, O. Lattice Oxygen Exchange in Rutile IrO2during the Oxygen Evolution Reaction. *J. Phys. Chem. Lett.* **2020**, *11*, 5008−5014.
(73) Marshall, A. T.; Haverkamp, R. G. Electrocatalytic Activity of IrO2-RuO2 Supported on Sb-Doped SnO2 Nanoparticles. *Electrochim. Acta* **2010**, *55*, 1978−1984.
(74) Oh, H.-S.; Nong, H. N.; Reier, T.; Gliech, M.; Strasser, P. Oxide-Supported Ir Nanodendrites with High Activity and Durability for the Oxygen Evolution Reaction in Acid PEM Water Electrolyzers. *Chem. Sci.* **2015**, *6*, 3321−3328.
(75) Liu, G.; Xu, J.; Wang, Y.; Wang, X. An Oxygen Evolution Catalyst on an Antimony Doped Tin Oxide Nanowire Structured Support for Proton Exchange Membrane Liquid Water Electrolysis. *J. Mater. Chem. A* **2015**, *3*, 20791−20800.
(76) Chen, G.; Bare, S. R.; Mallouk, T. E. Development of Supported Bifunctional Electrocatalysts for Unitized Regenerative Fuel Cells. *J. Electrochem. Soc.* **2002**, *149*, A1092.
(77) Reier, T.; Teschner, D.; Lunkenbein, T.; Bergmann, A.; Selve, S.; Kraehnert, R.; Schlögl, R.; Strasser, P. Electrocatalytic Oxygen Evolution on Iridium Oxide: Uncovering Catalyst-Substrate Interactions and Active Iridium Oxide Species. *J. Electrochem. Soc.* **2014**, *161*, F876−F882.
(78) Kamegaya, Y.; Sasaki, K.; Oguri, M.; Asaki, T.; Kobayashi, H.; Mitamura, T. Improved Durability of Iridium Oxide Coated Titanium Anode with Interlayers for Oxygen Evolution at High Current Densities. *Electrochim. Acta* **1995**, *40*, 889−895.
(79) Jovanovič, P.; Stojanovski, K.; Bele, M.; Dražić, G.; Koderman Podboršek, G.; Suhadolnik, L.; Gaberšček, M.; Hodnik, N. Methodology for Investigating Electrochemical Gas Evolution Reactions: Floating Electrode as a Means for Effective Gas Bubble Removal. *Anal. Chem.* **2019**, *91*, 10353−10356.

https://dx.doi.org/10.1021/acscatal.0c04741
ACS Catal. 2021, 11, 670−681